

# On the Numerical Simulation of Airflow and Clouds over Mountainous Terrain

E. C. Nickerson

National Oceanic and Atmospheric Administration, Atmospheric Physics and Chemistry Laboratory, Boulder, Colorado 80303, USA

(Manuscript received 5.1.1979, in revised form 20.4.1979)

## Abstract:

A mesoscale model has been developed designed with the capability of simulating moist, non-precipitating flow over mountainous terrain. The model makes use of a transformed sigma coordinate system to increase the vertical resolution in the planetary boundary layer. A preliminary evaluation of the performance of the model has been obtained from simulations of airflow and orographically induced cloud cover over the island of Hawaii.

## Zusammenfassung: Über die numerische Simulation von Strömung und Wolken über Gebirgen

Ein mesoskaliges Modell wurde entwickelt, das es erlaubt, die Strömung über gebirgigem Untergrund unter Berücksichtigung der Feuchte, aber ohne Niederschlag, zu simulieren. Das Modell benutzt ein transformiertes  $\sigma$ -Koordinaten-System um die vertikale Auflösung in der Grenzschicht zu erhöhen. Das Modell wurde getestet durch eine Simulation der Strömung und der orographischen Wolken über der Insel Hawaii.

## Résumé: Sur la simulation numérique de l'écoulement d'air et des nuages au-dessus de terrains montagneux

On a développé un modèle à mésoéchelle, qui permet de simuler l'écoulement de l'air au-dessus d'un terrain montagneux en tenant compte de l'humidité mais sans précipitations. Le modèle utilise une coordonnée  $\sigma$  transformée, en vue d'accroître la résolution verticale dans la couche-limite planétaire. Un test du modèle a été réalisé en simulant l'écoulement de l'air et les nuages orographiques au-dessus de l'île de Hawaii.

## 1 Introduction

This paper describes a mesoscale model designed to simulate airflow and non-precipitating orographic clouds over irregular terrain. According to REED (1977), numerical models on an operational basis are now capable of reasonably accurate 72-hour forecasts of synoptic scale flow patterns. However, significant improvements in local forecasts will require the development and implementation of meso- $\alpha$  models (e. g. scales 200–2000 km in horizontal extent) such as those of DANARD (1971), PERKEY (1976) and also meso- $\beta$  models such as those of ANTHES and WARNER (1974), TAPP and WHITE (1976), and MAHRER and PIELKE (1977) that seek to resolve scales 20–200 km in horizontal extent.

The development of a mesoscale model requires that some fundamental decisions be made regarding parameterizations of sub-grid scale and boundary layer processes. In order to provide for increased vertical resolution at the lower boundary and still to retain the advantages of a uniform grid, a transformed sigma system was developed and incorporated into the model. This "nu" coordinate places four of the fifteen computational levels within the lowest kilometer, with the lowest grid level approximately 18

meters above the surface. The decision to explicitly resolve the vertical structure of the planetary boundary layer is in accordance with the "merged" approach to atmospheric modeling advocated by PRIESTLY and TAYLOR (1972).

Model validation is an especially important part of a mesoscale model development program. The island of Hawaii was selected for a modeling study because repetitive meteorological conditions over the relatively smooth topography that extends from sea level to 4.2 km are responsible for large horizontal variations in rainfall. Hawaii has an extensive history of scientific scrutiny (MORDY et al. 1957, LAVOIE et al. 1967, and TAKAHASHI 1977). Its location under conditions of strong trade wind flow far removed from other orographic effects reduces the contamination of the interior model results by conditions imposed at the lateral boundaries. Furthermore, the repetitive nature of the meteorological conditions permits the use of climatological data to partially assess the accomplishments and deficiencies of the model.

## 2 The model

The basic equations for the nu coordinate system are as follows:

$$\frac{\partial U}{\partial t} = -\frac{\partial(Uu)}{\partial x} - \frac{\partial(Uv)}{\partial y} - \frac{1}{\sigma'} \frac{\partial(\sigma' U \bar{v})}{\partial \nu} + fV + \left( \phi - \frac{RT^* \sigma \pi}{P} \right) \frac{\partial \pi}{\partial x} - \frac{\partial(\pi \phi)}{\partial x} + F_U \quad (1)$$

$$\frac{\partial V}{\partial t} = -\frac{\partial(Vu)}{\partial x} - \frac{\partial(Vv)}{\partial y} - \frac{1}{\sigma'} \frac{\partial(\sigma' V \bar{v})}{\partial \nu} - fU + \left( \phi - \frac{RT^* \sigma \pi}{P} \right) \frac{\partial \pi}{\partial y} - \frac{\partial(\pi \phi)}{\partial y} + F_V \quad (2)$$

$$\frac{\partial S}{\partial t} = -\frac{\partial(Su)}{\partial x} - \frac{\partial(Sv)}{\partial y} - \frac{1}{\sigma'} \frac{\partial(\sigma' S \bar{v})}{\partial \nu} + F_S \quad (3)$$

$$\frac{\partial W}{\partial t} = -\frac{\partial(Wu)}{\partial x} - \frac{\partial(Wv)}{\partial y} - \frac{1}{\sigma'} \frac{\partial(\sigma' W \bar{v})}{\partial \nu} + F_W \quad (4)$$

$$\frac{\partial \pi}{\partial t} = - \int_0^1 \left( \frac{\partial U}{\partial x} + \frac{\partial V}{\partial y} \right) \sigma' d\nu \quad (5)$$

$$\bar{v} = \frac{1}{\pi \sigma'} \int_0^{\nu} \sigma' \left( \frac{\partial \pi}{\partial t} + \frac{\partial U}{\partial x} + \frac{\partial V}{\partial y} \right) d\nu^* \quad (6)$$

$$\frac{\partial \phi}{\partial \bar{p}} = -C_p \theta (1 + 0.61 q_v) \quad (7)$$

where  $U = \pi u$ ,  $V = \pi v$ ,  $W = \pi(q_v + q_{cw})$ ,

$$S = \pi (\ln(T/\bar{p}) + L q_v / C_p T), \quad (8)$$

and where  $\pi = P_S - P_T$ , the difference between the pressure at the lower boundary,  $P_S$ , and the pressure at the top of the model,  $P_T$ .

The vertical coordinate,  $\nu$ , was obtained by transforming the conventional sigma coordinate in the following manner,

$$\sigma = (4\nu - \nu^4)/3 \quad (9)$$

where  $\sigma = (P - P_T)/\pi$ . Equation (9) represents a simple ad hoc transformation which not only has vertical distances ranging from zero to unity as in the sigma system, but which satisfies the condition noted

by DE RIVAS (1972), that  $d\sigma/d\nu$  must be finite over the entire domain and must be equal to zero at  $\nu = \sigma = 1$  in order to assure second order accuracy in the discretization scheme.

We have also made the following definitions:

$$\begin{aligned}\sigma' &= d\sigma/d\nu & \phi &= gz \\ \dot{\nu} &= d\nu/dt & T^* &= T(1 + 0.61 q_v) \\ \hat{P} &= (P/P_0)^\kappa & L &= 597.3 - 0.566(T - 273.16) \\ \theta &= T/\hat{P}\end{aligned}$$

Here  $q_v$  and  $q_{cw}$  represent the mixing ratio for water vapor and cloud water, respectively. For all calculations reported on in this paper,  $p_0$  is 1013 mb, and  $P_T$  is zero.

Temperature is not explicitly predicted by the model, but must be extracted from the predicted value of the entropy variable,  $S$ . If the air is saturated, the mixing ratio is a known function of temperature, and (8) becomes a transcendental equation for the temperature,  $T_s$ , corresponding to saturation with respect to liquid water. If on the other hand the air is unsaturated, the mixing ratio in (8) is replaced by  $W/\pi$  and the temperature is solved for directly, using the temperature at the previous time step to account for the temperature dependence of the latent heat. In the present formulation of the model no conversion of cloud water to precipitation is included, and saturation with respect to liquid water is required for any cloud water to be present.

In order to determine the temperature and moisture variables, we first compute  $T_s$  and  $q_{vs}$ , the saturation temperature and its corresponding mixing ratio (the NEWTON-RAPHSON technique is currently being used). Temperature and mixing ratio are then arrived at in accordance with the following criteria:

$$\left. \begin{aligned}q_v &= q_{vs} \\ q_{cw} &= W/\pi - q_{vs} \\ T &= T_s\end{aligned} \right\} W > \pi q_{vs}$$

$$\left. \begin{aligned}q_v &= W/\pi \\ q_{cw} &= 0 \\ T &= T_{uns}\end{aligned} \right\} W \leq \pi q_{vs}$$

where  $T_{uns}$  is again the solution of (8) for given  $S$ ,  $\pi$ , and  $q_v$ .

The saturation vapor pressure with respect to water,  $e_s$ , used to compute  $q_{vs}$  is taken from MURRAY (1967),

$$e_s = 6.11 \exp [17.27 (T - 273.16)/(T - 35.86)]$$

### 3 Lower boundary conditions

A constant flux layer is presumed to exist between the lower boundary (with roughness length  $z_0$ ), and the first grid point above the surface,  $z = h$ . The friction velocity and surface fluxes of sensible and latent heat are computed using the BUSINGER-DYER surface layer formulation (see NICKERSON and SMILEY, 1975).

$$\begin{aligned}u/u_* &= F(z/L, z/z_0) \\ (\theta - \theta_0) u_* / (-w' \theta'_0) &= G(z/L, z/z_0) \\ (q_v - q_{v,0}) u_* / (-w' q'_{v,0}) &= G(z/L, z/z_0)\end{aligned}$$

where  $L$  is the MONIN-OBUKHOV length, and where the functional forms for  $F$  and  $G$  depend on the density stratification.

In order to link the theoretical formulation with the discretization scheme used in the model it is convenient to define a bulk RICHARDSON number for the surface layer,

$$Ri_B = hg(\theta_h - \theta_0)/\theta_h u_h^2$$

where the subscript  $h$  denotes the value at the height  $h$ .

If the MONIN-OBUKHOV length is written as

$$L = -u_*^3 \theta_h / kg w' \theta'_0$$

where  $k$  is the KÁRMÁN constant, we then obtain the following equation valid at the height  $z = h$ :

$$Gz/L - kF^2 Ri_B = 0 \quad (10)$$

For a given value of bulk RICHARDSON number and surface roughness, (10) becomes a transcendental equation for  $z/L$ , where  $z$  is now  $h$ . After solving (10) for  $h/L$ , we obtain expressions for the surface fluxes.

$$u_* = u_h/F$$

$$w' \theta'_0 = u_h (\theta_0 - \theta_h)/FG$$

$$w' q'_0 = u_h (q_0 - q_h)/FG$$

For unstable conditions (i.e.,  $\theta_0 - \theta_h > 0$ ), the functions  $F$  and  $G$  have the form

$$kF = \ln(z/z_0) + \ln \left[ \frac{(\xi_0^2 + 1)(\xi_0 + 1)^2}{(\xi^2 + 1)(\xi + 1)^2} \right] + 2 \tan^{-1} \xi - 2 \tan^{-1} \xi_0$$

$$kG/R = \ln(z/z_0) - 2 \ln \left( \frac{\eta^2 + 1}{\eta_0^2 + 1} \right)$$

where  $R$  is a constant equal to .74, and where the results of BENOIT (1977) have been used to eliminate a computational difficulty that arises when  $(\xi - 1)$  is very close to zero. The following definitions have also been made.

$$\xi = (1 - \gamma z/L)^{1/4}$$

$$\xi_0 = (1 - \gamma z_0/L)^{1/4}$$

$$\eta = (1 - \gamma'' z/L)^{1/4}$$

$$\eta_0 = (1 - \gamma'' z_0/L)^{1/4}$$

The constants  $\gamma$  and  $\gamma''$  have been set equal to 15 and 9, respectively.

For mildly stable conditions (i.e.,  $z/L < 1$ ), the functions  $F$  and  $G$  have the form

$$kF = \ln(z/z_0) + \beta z/L$$

$$kG = R \ln(z/z_0) + \beta z/L$$

where  $\beta = 4.7$ .

For  $z/L > 1$ , the functions  $F$  and  $G$  are obtained from profiles given by WEBB (1970).

$$kF = \beta \ln(z/L) + \ln(z/z_0) + \beta$$

$$kG = (1 + \beta - R) \ln(z/L) + R \ln(z/z_0) + \beta$$

At the present stage of model development the surface temperature and mixing ratio are specified initially and not allowed to change during the course of the model run.

#### 4 Planetary boundary layer

A boundary layer is presumed to exist between  $z_B = h$ , the first grid point above the surface and  $z_A$ , some specified height where the winds become decoupled from surface layer effects. At the present time  $z_A$  is set equal to one kilometer. Exchange coefficients for momentum,  $K(u)$ , and for the temperature and moisture,  $K(T)$  at  $z_B = h$  are given by  $u_*/(F')_B$  and  $u_*/(G')_B$ , respectively. Between  $z_A$  and  $z_B$ , the coefficients are computed in accordance with the profile given by O'BRIAN (1970).

$$K = K_A + [(z - z_A)^2 / (\Delta z)^2] [K_B - K_A + (z - z_B) (K'_B + 2(K_B - K_A)/\Delta z)]$$

The prime denotes a derivative with respect to  $z$ , and  $\Delta z = (z_A - z_B)$ . Both  $K(u)$  and  $K(T)$  are set equal to zero for heights greater than  $z_A$ . Moreover, horizontal friction is not explicitly included in the model except at the top and on the lateral boundaries.

The frictional terms in (1), (2), (3), and (4) are written as

$$F_U = A \frac{\partial}{\partial \nu} \left( AK(u) \frac{\partial U}{\partial \nu} \right)$$

$$F_V = A \frac{\partial}{\partial \nu} \left( AK(u) \frac{\partial V}{\partial \nu} \right)$$

$$F_S = A \frac{\partial}{\partial \nu} \left( AK(T) \frac{\partial S}{\partial \nu} \right)$$

$$F_W = A \frac{\partial}{\partial \nu} \left( AK(T) \frac{\partial W}{\partial \nu} \right)$$

where  $A = -gp/RT \pi \sigma'$ .

At the lower boundary ( $\nu = \sigma = 1$ )

$$AK(u) \frac{\partial U}{\partial \nu} = \pi u_*^2 \cos \alpha$$

$$AK(u) \frac{\partial V}{\partial \nu} = \pi u_*^2 \sin \alpha$$

$$AK(T) \frac{\partial S}{\partial \nu} = \pi \left( \frac{Q_s \bar{P}}{T} + \frac{LQ_e}{C_p} \right)$$

$$AK(T) \frac{\partial W}{\partial \nu} = \pi Q_e$$

where  $\tan \alpha = V_h/U_h$ , the ratio of the two wind components at the first grid point above the surface, and where the surface fluxes of heat and moisture  $Q_s$  and  $Q_e$  are given by

$$\pi Q_s = (\theta_0 - \theta_h) \sqrt{U_h^2 + V_h^2} / FG$$

$$\pi Q_e = (q_0 - q_h) \sqrt{U_h^2 + V_h^2} / FG$$

## 5 Model grid

The vertical grid consists of 15 equally spaced levels in the Nu coordinate system. With reference to Figure 1, the variable  $\nu$  is defined at the circled levels, and all other variables are defined at the crosses. Vertical distances in the Nu coordinate system range from zero to unity, just as in the sigma system.

A staggered grid is used to reduce the truncation errors on the level Nu surfaces (see ANTHES and WARNER, 1974). For the runs reported on this paper,  $\Delta x$  and  $\Delta y$  have both been set equal to 10 km. With 26 grid points in each direction, this corresponds to an area 250 km on a side.

	Grid Level	Condition on Nu
■		$\nu=0$
×	1	
○		
×	2	
○		
×	3	
○		
×	4	
•		
•		
•		
×	13	
○		
×	14	
○		$\Delta\nu=1/15$
×	15	
■		$\nu=1$

- Figure 1  
Vertical grid used in the model calculations
- Bild 1  
Das in den Modellrechnungen benutzte vertikale Gitter

## 6 Time Differencing

Centered differences are used to represent the time derivative, except that every fifth time-step a Time and Space Uncentered MATSUNO procedure is introduced (see ARAKAWA and MINTZ, 1974). The time increment,  $\Delta t$ , has been set equal to 10 sec.

## 7 Space Differencing

The horizontal grid and the discretization scheme that follows are based on ANTHES and WARNER (1974). The staggered grid has a smaller truncation error than a non-staggered grid. Perhaps more important, however, is the fact that boundary values of the velocity components appear only in the flux terms of the momentum equations and not in calculations using the continuity equation.

The finite difference analogs of Equations (1) to (7) are given in Appendix A. The vertical velocity,  $dz/dt$ , is also calculated in order to assist in the interpretation of the results. This is especially important for computations above steep mountain slopes where the usual approximation  $w = -\omega/\rho g$  can give the wrong sign.

## 8 Smoothing operator

A smoothing operator has been applied to the predicted fields of  $\pi u$ , and  $\pi v$  (see SHAPIRO, 1970).

A smooth value of a variable,  $\lambda$ , is defined by

$$\tilde{\lambda}_{i,j} = (\lambda_{i+1,j+1} + \lambda_{i-1,j+1} + \lambda_{i+1,j-1} + \lambda_{i-1,j-1} + 4\lambda_{i,j})/8$$

## 9 Boundary conditions

At the upper boundary ( $\sigma = \nu = 0$ )  $\dot{\nu}$  is set to zero. This is a reasonable condition when  $P_T = 0$ , but may lead to difficulties when  $P_T$  is greater than 100 mb. Quantities such as wind and temperature are set equal to values at the grid point immediately below the top of the model. Actual values chosen are not of great importance, however, since the equations are written in flux form (i. e.  $\dot{\nu}\pi u$ ) and the terms containing boundary values vanish on the upper boundary due to the condition on  $\dot{\nu}$ .

The thermodynamic variables are specified at all boundaries. Winds are specified on inflow boundaries and extrapolated from interior values on outflow boundaries. In addition, a viscous term is added to the predictive equations for  $U$  and  $V$  on the lateral and top boundaries. This is applied only at the first two interior grid points and is a simple Laplacian operator evaluated at the  $(n-1)$  time level.

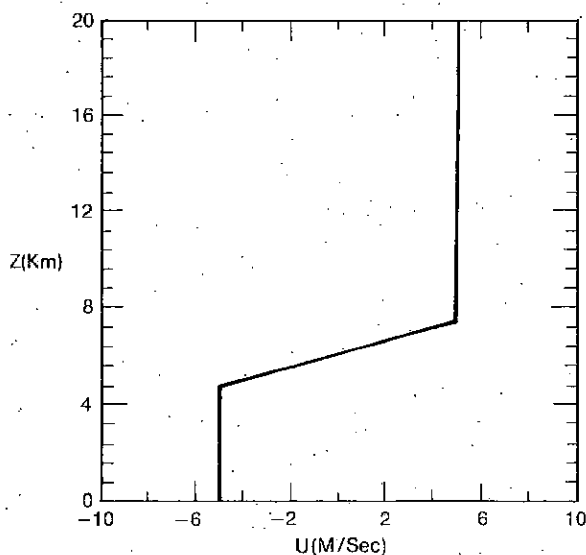
## 10 Initial conditions

During the fully developed and undisturbed trade wind regime, the air in the lowest few kilometers of the Eastern Pacific high has ample time to adjust to conditions at the ocean surface before encountering land. Under those conditions, topographical features or other sources of horizontal variability outside the computational domain ought to have little influence on the island weather. Representative inflow boundary data could therefore be obtained from an undisturbed trade wind sounding. The sounding station at Lihue, Kauai would probably provide the most representative data on a routine basis.

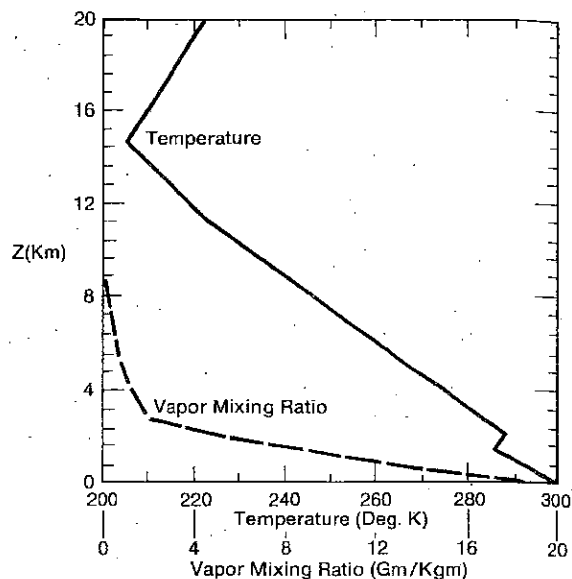
Initial conditions of wind, temperature, and mixing ratio for the numerical calculations are shown in Figures 2 and 3. The initial wind field contains easterlies at low levels and westerlies aloft. The temperature at the lower boundary remains constant in time, and decreases linearly with altitude from its sea level value of 299 K.

The temperature at the lower boundary has not been related to land use or vegetation; however, limited use of that information has been made in specifying the roughness length and mixing ratio at the surface. Vegetation and soil conditions were estimated from U.S.G.S. woodland print topographic charts. Roughness lengths were then obtained from PRIESTLEY (1959), SELLERS (1966), and SUTTON (1953).

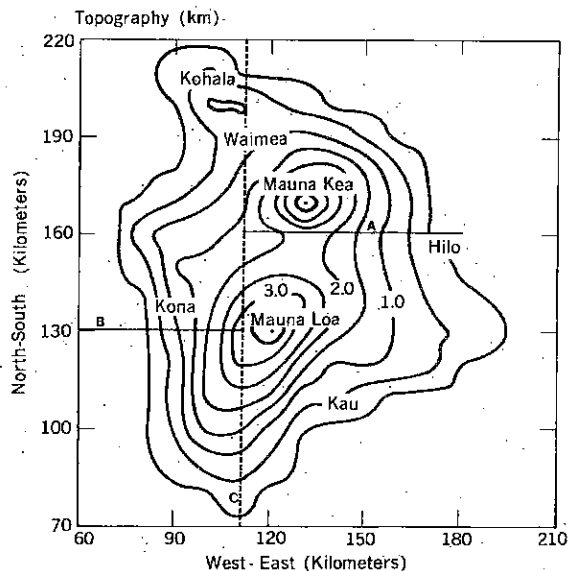
Terrain heights used in the model calculation are actual values obtained from U.S.G.S. maps and have not been smoothed. The topography shown in Figures 4 and 5 is present in the model from the moment the calculations begins and does not build up gradually during a start-up period as is the case in the model of MAHRER and PIELKE (1977).



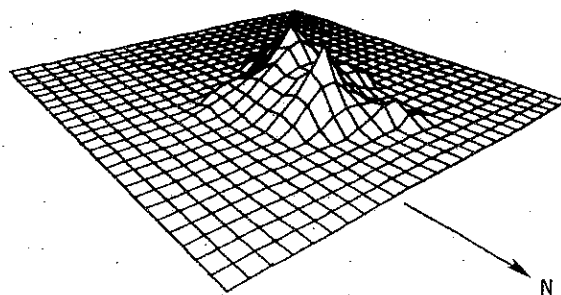
- **Figure 2** Initial  $u$  profile over open water.  $v$  is initially zero everywhere, and both components are set to zero at the island surface.
- **Bild 2** Anfangsprofil von  $u$  über offenem Wasser.  $v$  ist im Anfangszustand überall Null. Beide Komponenten sind Null an der Oberfläche der Insel.



- **Figure 3** Initial soundings of temperature and vapor mixing ratio over open water.
- **Bild 3** Anfangsprofile vom Temperatur und Mischungsverhältnis des Wasserdampfes über offenem Wasser

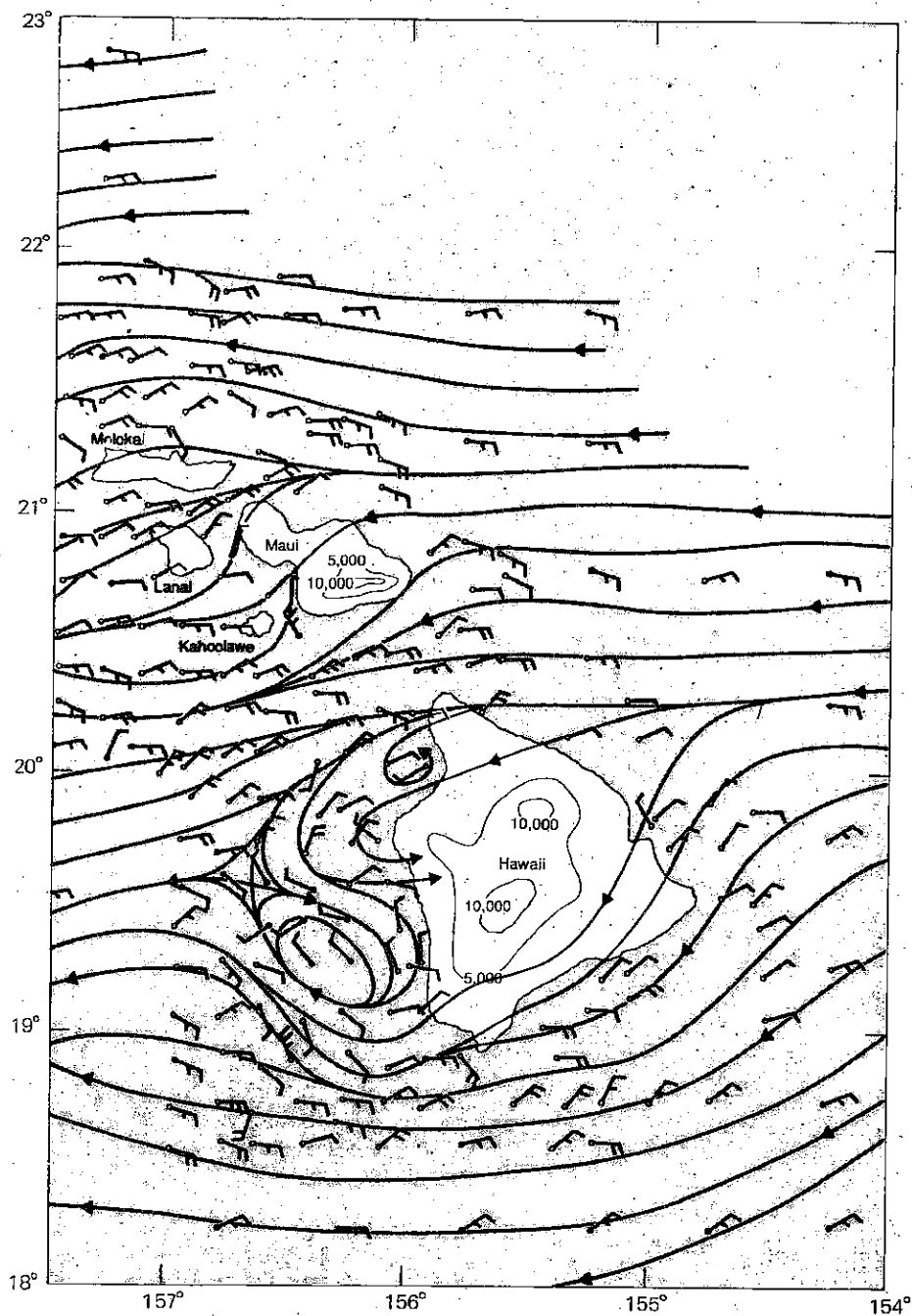


- **Figure 4** Elevation isopleths for Hawaii. The locations of the vertical cross sections corresponding to Figures 13–16 are also shown.
- **Bild 4** Höhenlinien für Hawaii. Die Orte der Querschnitte der Bilder 13 bis 16 sind eingezeichnet.



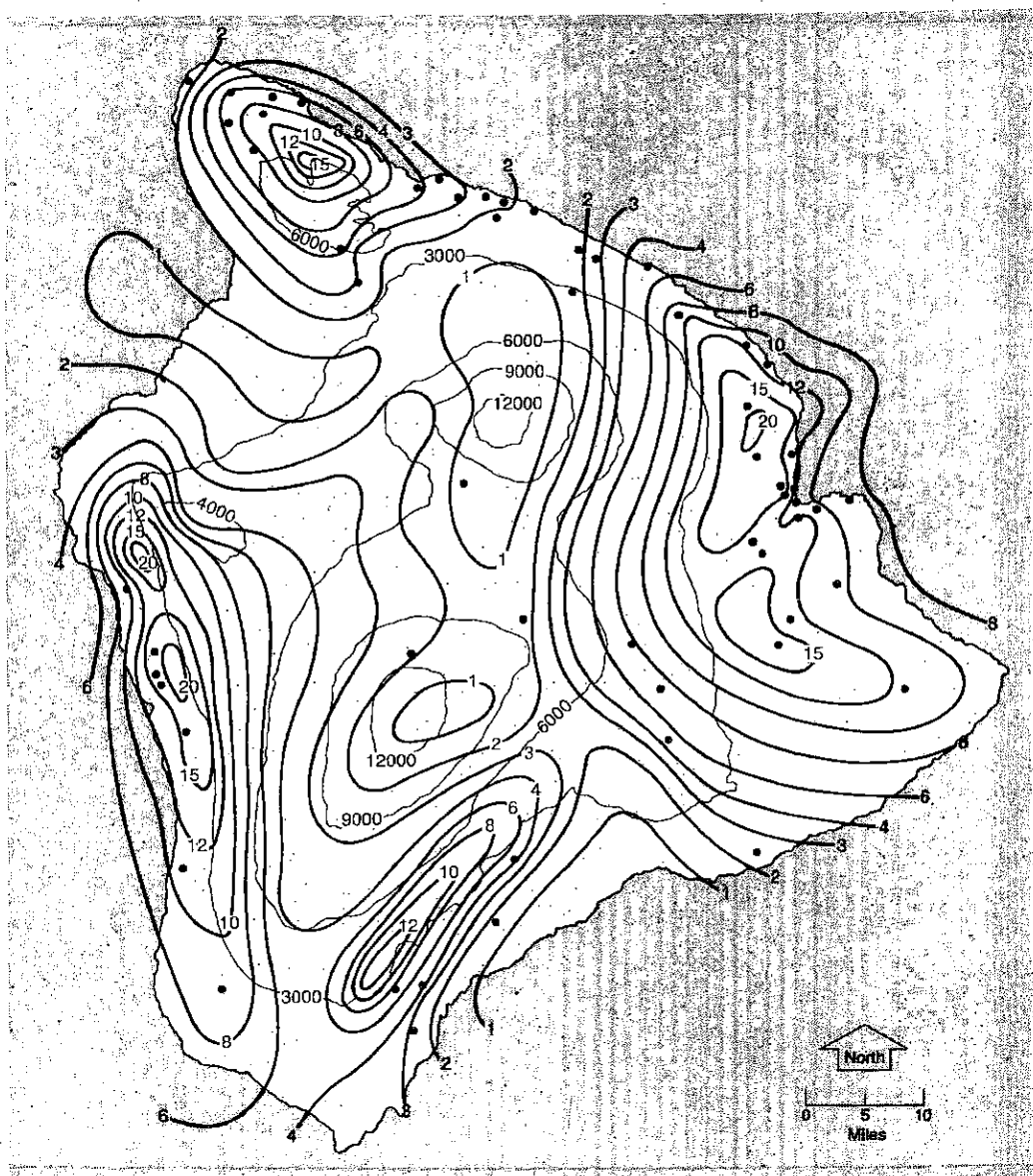
- **Figure 5** Perspective view of Hawaii terrain. Locations of individual grid points coincide with the intersections of north-south and east-west lines. The view is from northeast ( $50^\circ$ ) looking southwest.
- **Bild 5** Perspektivische Darstellung der Hawaii-orographie. Die Orte der Gitterpunkte fallen mit den Schnittpunkten der nord-südlich und west-östlich verlaufenden Linien zusammen. Man blickt hier von NE ( $50^\circ$ ) nach SW





• Figure 6 Composite surface wind field over Hawaiian waters taken from unpublished Weather Bureau Data, Honolulu (1968) after PATZERT (1970).

• Bild 6 Zusammengesetztes Feld des Windes nahe der Oberfläche des Meeres in der Umgebung von Hawaii nach PATZERT (1970)



- Figure 7 Rainfall for the period 11 July to 24 August 1965 from LAVOIE (1966). Isohyets are labeled in inches.
- Figure 7 Niederschlagsfeld (Isohyeten in inches) für die Zeit vom 11.7. bis 24.8.1965 nach LAVOIE (1966)

## 11 Hawaiian climatology

The importance of the twin peaks Mauna Loa and Mauna Kea to the island meteorology cannot be overemphasized. Leeward convergence of the anti-cyclonic flow south of Mauna Loa and the cyclonic flow north of Mauna Kea results in a suppression of the vortex streets commonly observed in the cloud patterns downwind of tall islands. This zone of horizontal convergence (see Figure 6, taken from

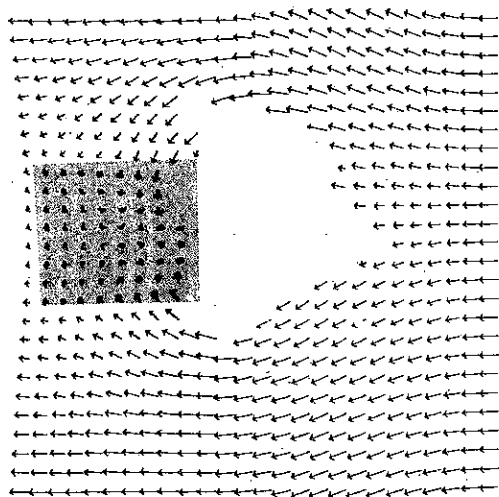
PATZERT, 1970) apparently interacts with the sea breeze to produce a secondary rainfall maximum on the leeward (Kona) coast (CHOPRA, 1973). The Kona rainfall maximum and the sharp demarcation between wet and dry areas are vividly illustrated in Figure 7, which shows LAVOIE's (1966) summer rainfall distribution. Despite the occurrence of different wind regimes associated with winter storm systems, the locations of the precipitation maxima and minima in Figure 7 also coincide with those of the annual pattern.

The interaction of the prevailing trade winds with the land/sea breezes and the mountain/valley wind systems results in distinctly different diurnal rainfall distributions on the windward and leeward sides of the island (SCHROEDER et al. 1977). At lower elevations on the windward coast, the interaction of the downslope drainage wind with the onshore trade wind produces a nocturnal rainfall maximum. At higher elevations, however, surface heating assumes a more dominant role and the rainfall distribution shifts to an afternoon maximum. The leeward coast also experiences an afternoon rainfall maximum, reflecting the importance of land/sea breezes and the absence of the prevailing trade winds.

## 12 Results

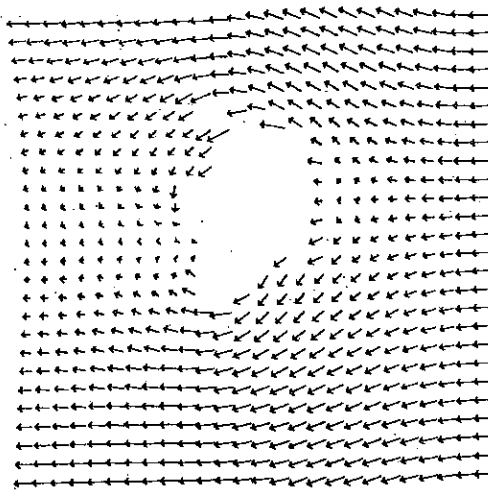
All model results reported in this section were calculated in a terrain-following coordinate system. However, it is often more convenient to display the data using height as the vertical coordinate. Since the height of each grid point is known, the value of a quantity at some intermediate location is calculated using linear interpolation between two computational levels.

Horizontal windfields corresponding to elevations of 100, 1000, and 4000 meters above sea level are shown in Figures 8–10. The low level convergence zone on the left side of Figure 8 is of particular interest, and an expanded view of the convergence zone is shown in Figure 11. Although the computed winds do not contain all the details of the composite wind field shown in Figure 6, the model did succeed in reproducing some of the primary features including the leeward convergence zone.



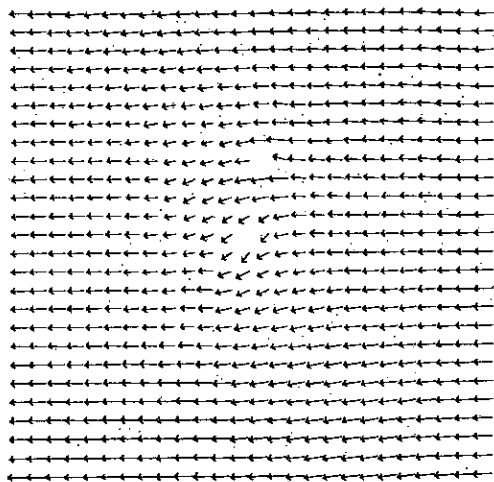
• Figure 8 Vector wind field 100 m above sea level after 1.4 hr. of model time. See Figure 11 for an expanded view of the shaded area.

• Bild 8 Windfeld 100 m über dem Meeresniveau nach 1,4 h Modellzeit. In Bild 11 ist das schraffierte Gebiet vergrößert dargestellt

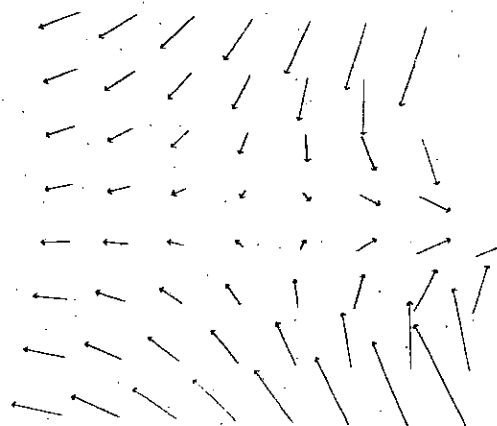


• Figure 9 Vector wind field 1000 m above sea level after 1.4 hr. of model time.

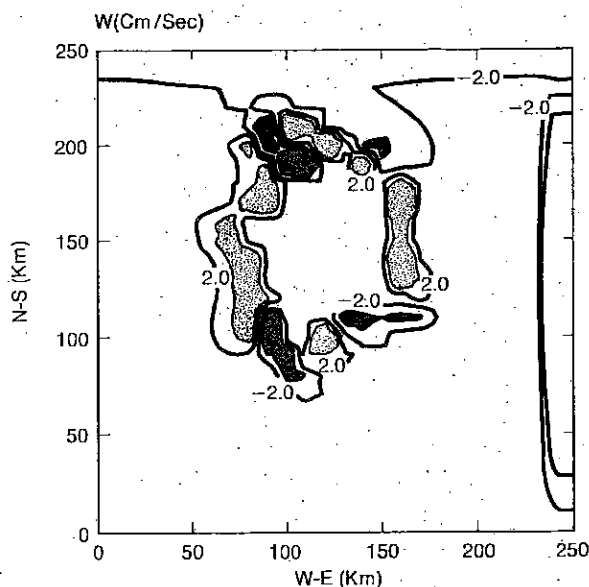
• Bild 9 Windfeld 1000 m über dem Meeresniveau nach 1,4 h Modellzeit



- **Figure 10** Vector wind field 4000 m above sea level after 1.4 hr. of model time
- **Bild 10** Windfeld 4000 m über dem Meeresniveau nach 1,4 h Modellzeit



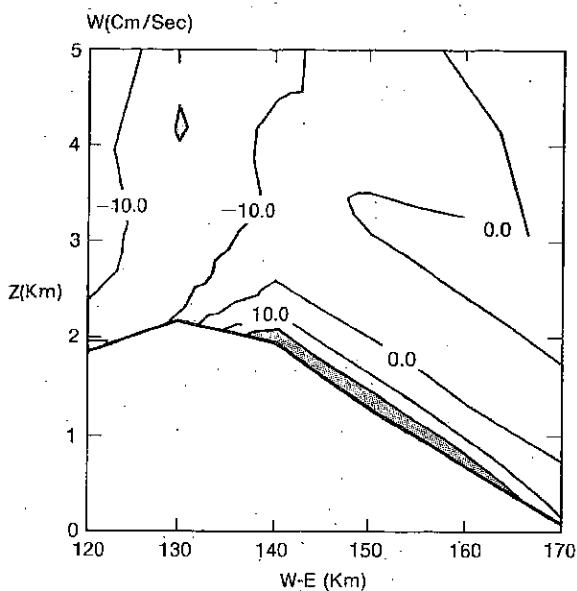
- **Figure 11** Expanded view of Kona convergence zone corresponding to the shaded area of Figure 8
- **Bild 11** Ausschnittsvergrößerung des schraffierten Teiles von Bild 8, dies ist die Konvergenzzone von Kona



- **Figure 12**  
Vertical velocity at 1000 m above sea level after 1.4 hr. of model time. Ascending and descending motions in excess of 5 cm/s. are indicated by the shaded and checkered areas, respectively
- **Bild 12**  
Vertikalgeschwindigkeit in 1000 m über dem Meeresniveau nach 1,4 h Modellzeit. Aufsteigende und absinkende Bewegung, die 5 cm/s übersteigt, ist dargestellt in den gepunkteten und schraffierten Gebieten

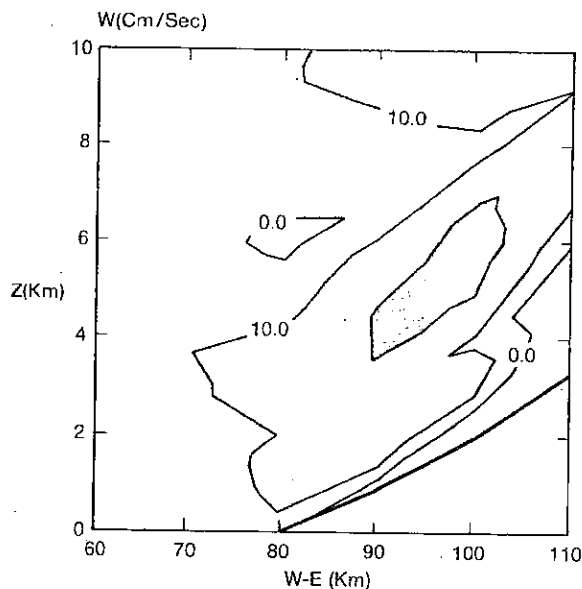
The numerical computations indicate that the effects of the island on the airflow may be felt 50 to 100 km from land. A more accurate determination of the island influence region would require the calculations to be performed over a larger horizontal domain.

Primary regions of convergence and divergence are quite apparent in the horizontal wind fields shown in Figures 8–10. And yet there must be other, more subtle horizontal convergence patterns responsible for



● **Figure 13** West-east cross sections of vertical velocity through the saddle cloud (section A) after 1.4 hr. of model time. Shaded areas indicate values in excess of 20 cm/s.

● **Bild 13** W-E-Querschnitt der Vertikalgeschwindigkeit durch die Sattel-Wolke (Schnitt A auf Bild 4) nach 1,4 h Modellzeit. In den geschummerten Gebieten gibt es Werte über 20 cm/s

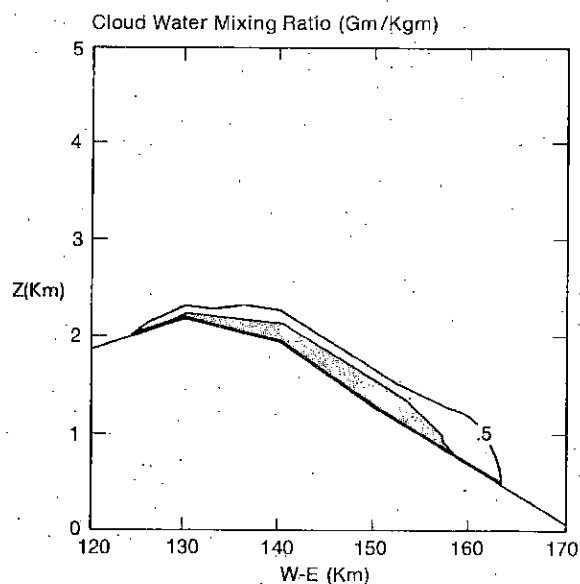


● **Figure 14** West-east cross section of vertical velocity through the Kona convergence zone (section B) after 1.4 hr. of model time. Shaded areas indicate values in excess of 20 cm/s

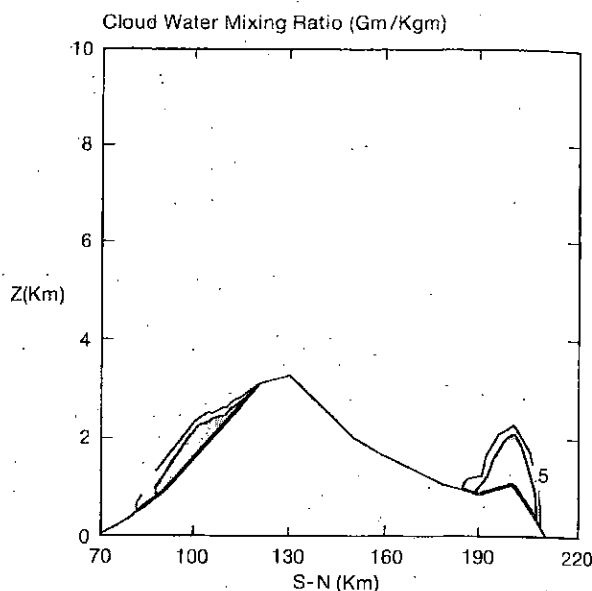
● **Bild 14** W-E-Querschnitt der Vertikalgeschwindigkeit durch die Kona-Konvergenz-Zone (Schnitt B auf Bild 4) nach 1,4 h Modellzeit. In dem geschummerten Gebiet gibt es Werte über 20 cm/s

the extreme variability in the precipitation distribution of Figure 7. These terrain-induced regions of horizontal convergence become much more obvious when we examine the vertical motion field at an elevation of 1000 m above sea level as shown in Figure 12. An examination of figure 7 shows that all the major precipitation maxima are well correlated with the areas of rising motion in Figure 12. Areas of strong descent in Figure 12 also have their counterparts in the precipitation maxima of Figure 7. The Kau and South Kohala desert areas in particular are under the influence of sinking air, although the model calculations seem to have the North Kona rising motion intruding upon the South Kohala desert. The orographically forced upward motion on the windward slopes is relatively shallow (see Figure 13), but in Figure 14 we see that the leeward convergence zone is associated with a broad area of gradual ascent.

The correlation between the vertical motion field and the observed precipitation does not carry over to the calculated cloud over distribution nearly as well. A vertical cross section through the Mauna Loa-Mauna Kea saddle cloud (Figure 15) shows a cloud only half the thickness of that observed by MORDY et al. (1957). It would probably be necessary to include warm rain processes and a convective parameterization scheme in order to simulate the observed cloud cover more realistically. The lack of any cloud cover in the Kona convergence zone should probably not cause any great surprise in view of the model's neglect of cumulus processes. The calculated North Kohala cloud (Figure 16), on the other hand appears deeper than the saddle cloud and representative of the typical Kohala cloud.



- **Figure 15** Cloud water mixing ratio through the saddle cloud corresponding to the same cross section as Figure 13. Shaded areas indicate values in excess of 1 g/kg.
- **Bild 15** Flüssigwassergehalt in der Sattel-Wolke in demselben Querschnitt wie bei Bild 13. In dem geschummerten Gebiet gibt es Werte von über 1 g/kg



- **Figure 16** South-north cross section of cloud water mixing ratio (section C) after 1.4 hr. of model time. Shaded areas indicate values in excess of 1 g/kg.
- **Bild 16** S-N-Querschnitt des Flüssigwassergehaltes (Schnitt C auf Bild 4) nach 1,4 h Modellzeit. In den geschummerten Gebieten gibt es Werte von über 1 g/kg

### 13 Conclusion

A mesoscale model has been developed to simulate orographic clouds and modifications to air-flow caused by mountainous terrain. The model has demonstrated an ability to simulate not only some major features of the wind field over the island of Hawaii (i. e. the Kona convergence zone) but also the smaller scale regions of cloudiness and vertical motion associated with the distinctive climate zones found on the island. Hawaii offers a unique setting for the testing of mesoscale models of varying degrees of complexity.

### Acknowledgements

The author wishes to thank Dr. H. K. WEICKMANN and Dr. C. F. CHAPPELL of the Atmospheric Physics and Chemistry Laboratory, NOAA, for their encouragement, support, and guidance in developing the model. The graphics software necessary for viewing the output of a three-dimensional model was developed by Mr. E. L. MAGAZINER. Professors T. SCHROEDER and C. S. RAMAGE of the University of Hawaii at Manoa also contributed to our knowledge of Hawaiian meteorology. This work was sponsored in part by the Bureau of Reclamation under Contract No. 14-06-D-7676.

## References

- ANTHES, R. A. and T. T. WARNER, 1975: Prediction of mesoscale flows over complex terrain. ECOM Technical Report No. 5532, White Sands Missile Range, New Mexico 88002.
- ARAKAWA, A. and Y. MINTZ, 1974: The UCLA general circulation model. Notes distributed at the workshop, 25 March - 4 April 1974, Dept. of Meteorology, UCLA.
- BENOIT, R., 1977: On the integral of the surface layer profile - gradient functions. *J. Appl. Meteor.*, **16**: 859-860.
- CHOPRA, K. P., 1973: Atmospheric and oceanic flow problems introduced by islands. *Advances in Geophysics*, **16**, 297-421.
- DANARD, M., 1971: A numerical study of the effects of longwave radiation and surface friction on cyclone development. *Mon. Wea. Rev.*, **99**, 831-839.
- DE RIVAS, E. K., 1972: On the use of nonuniform grids in finite difference equations. *J. Comp. Phys.*, **10**, 202-210.
- LAVOIE, R. L., 1966: The warm rain project in Hilo, Hawaii, summer 1965. H.I.G.-66-5, Univ. of Hawaii.
- LAVOIE, R. L., et al., 1967: The warm rain project in Hawaii, *Tellus*, **19**, 347-461.
- MAHRER, Y., and R. A. PIELKE, 1977: A numerical study of airflow over irregular terrain. *Beitr. Phys. Atmosph.*, **50**, 98-113.
- MORDY, W. A., et al., 1957: Project Shower, an investigation on warm rainfall in Hawaii. *Tellus*, **9**, 471-590.
- MURRAY, F. W., 1967: On the computation of saturation vapor pressure. *J. Appl. Meteor.*, **6**, 203-204.
- NICKERSON, E. C. and V. E. SMILEY, 1975: Surface layer and energy budget parameterizations for mesoscale models. *J. Appl. Meteor.*, **14**, 297-300.
- O'BRIAN, J., 1970: On the vertical structure of the eddy exchange coefficient in the planetary boundary layer. *J. Atmos. Sci.*, **27**, 1213-1215.
- PATZERT, W. C., 1970: Eddies in Hawaiian waters. H.I.G.-69-9, University of Hawaii.
- PERKEY, D., 1976: A description and preliminary results from a fine mesh model for forecasting quantitative precipitation. *Mon. Wea. Rev.*, **104**, 1513-1526.
- PRIESTLEY, C. H. B., 1959: *Turbulent Transfer in the Lower Atmosphere*. University of Chicago Press, Chicago, 111.
- PRIESTLEY, C. H. B., and R. J. TAYLOR, 1972: On the assessment of surface heat flux and evaporation using large-scale parameters. *Mon. Wea. Rev.*, **100**, 81-92.
- REED, R. J., 1977: The development and status of modern numerical weather prediction. *Bull. Am. Meteor. Soc.*, **58**, 390-400.
- SCHROEDER, T. A., B. J. KILONSKY, and B. N. MEISNER, 1977: Diurnal variation in rainfall and cloudiness. Tech. Rept. No. 112, UHMET 77-03. University of Hawaii.
- SELLERS, W. D., 1966: *Physical Climatology*. Univ. of Chicago Press, Chicago, 111.
- SHAPIRO, R., 1970: Smoothing, filtering and boundary effects. *Rev. Geophys. Space Phys.*, **8**, 359-387.
- SUTTON, O. G., 1953: *Micrometeorology*, McGraw-Hill, New York.
- TAKAHASHI, T., 1977: Rainfall of Hilo, Hawaii. *J. Met. Soc., Japan*, **55**, 121-129.
- TAPP, M. C., and P. W. WHITE, 1976: A non-hydrostatic mesoscale model. *Q. J. Roy. Meteor. Soc.*, **102**, 277-296.
- WEBB, E. K., 1970: Profile relationships: The log-linear range and extension to strong stability. *Q. J. Roy. Meteor. Soc.*, **96**, 67-90.

## Appendix A

$$\left(\frac{\partial U}{\partial t}\right)_{i,j,k} = D_1(U) + D_2(U) + D_3(U) + fV + D_6(U)$$

$$\left(\frac{\partial V}{\partial t}\right)_{i,j,k} = D_1(V) + D_2(V) + D_3(V) - fU + D_7(V)$$

$$\left(\frac{\partial S}{\partial t}\right)_{i+1/2,j+1/2,k} = D_2(S) + D_4(S) + D_5(S)$$

$$\left(\frac{\partial W}{\partial t}\right)_{i+1/2,j+1/2,k} = D_2(W) + D_4(W) + D_5(W)$$

$$\left(\frac{\partial \pi}{\partial t}\right)_{i+1/2,j+1/2} = -\Delta\nu \sum_{k=1}^{15} \sigma' [D_8(U) + D_9(V)]$$

$$(\dot{\nu} \sigma' \pi)_{i+1/2,j+1/2,k-1/2} = -\Delta\nu \sum_{k^*=1}^k \sigma' \left[ \frac{\partial \pi}{\partial t} + D_8(U) + D_9(V) \right]$$

$$\phi_{i+1/2,j+1/2,k} = \phi_{i+1/2,j+1/2,k+1} + C_P [\theta_{k+1/2} (1 + 0.61 q_V)_{k+1/2} (\hat{P}_{k+1} - \hat{P}_k)_{i+1/2,j+1/2}]$$

where the following definitions have been made:

$$\begin{aligned} D_1(\lambda) = & -\frac{1}{4\Delta x} [(u_{i+1,j} + u_{i,j}) (\bar{\lambda}_{i+1/2,j+1/2} + \bar{\lambda}_{i+1/2,j-1/2}) \\ & - (u_{i,j} + u_{i-1,j}) (\bar{\lambda}_{i-1/2,j+1/2} + \bar{\lambda}_{i-1/2,j-1/2})] \\ & -\frac{1}{4\Delta y} [(v_{i,j+1} + v_{i,j}) (\bar{\lambda}_{i+1/2,j+1/2} + \bar{\lambda}_{i-1/2,j+1/2}) \\ & - (v_{i,j} + v_{i,j-1}) (\bar{\lambda}_{i+1/2,j-1/2} + \bar{\lambda}_{i-1/2,j-1/2})] \end{aligned}$$

$$D_2(\lambda) = \frac{1}{\sigma' \Delta\nu} [(\dot{\nu} \sigma' \lambda)_{k+1/2} - (\dot{\nu} \sigma' \lambda)_{k-1/2}]$$

$$D_3(\lambda) = \frac{\bar{A}_{i,j,k}}{(\Delta\nu)^2} [(\lambda_{k+1} - \lambda_k) (\bar{A}K(u))_{k+1/2} - (\lambda_k - \lambda_{k-1}) (\bar{A}K(u))_{k-1/2}]$$

$$\begin{aligned} D_4(\lambda) = & -\frac{1}{4\Delta x} [(U_{i+1,j+1} + U_{i+1,j}) (\lambda_{i+3/2,j+1/2} + \lambda_{i+1/2,j+1/2}) \\ & - (U_{i,j+1} + U_{i,j}) (\lambda_{i+1/2,j+1/2} + \lambda_{i-1/2,j+1/2})] \\ & -\frac{1}{4\Delta y} [(V_{i+1,j+1} + V_{i,j+1}) (\lambda_{i+1/2,j+3/2} + \lambda_{i+1/2,j+1/2}) \\ & - (V_{i+1,j} + V_{i,j}) (\lambda_{i+1/2,j+1/2} + \lambda_{i+1/2,j-1/2})] \end{aligned}$$

$$D_5(\lambda) = \frac{A_k}{(\Delta\nu)^2} [(\lambda_{k+1} - \lambda_k) (AK(T))_{k+1/2} - (\lambda_k - \lambda_{k-1}) (AK(T))_{k-1/2}]$$



$$D_6(U) = \frac{\bar{C}}{2\Delta x} [\pi_{i+1/2,j+1/2} - \pi_{i-1/2,j+1/2} + \pi_{i+1/2,j-1/2} - \pi_{i-1/2,j-1/2} \\ - \frac{1}{2\Delta x} (\pi\phi)_{i+1/2,j+1/2} - (\pi\phi)_{i-1/2,j+1/2} + (\pi\phi)_{i+1/2,j-1/2} \\ - (\pi\phi)_{i-1/2,j-1/2}]$$

$$D_7(V) = \frac{\bar{C}}{2\Delta y} [\pi_{i+1/2,j+1/2} - \pi_{i+1/2,j-1/2} + \pi_{i-1/2,j+1/2} - \pi_{i-1/2,j-1/2}] \\ - \frac{1}{2\Delta y} [(\pi\phi)_{i+1/2,j+1/2} - (\pi\phi)_{i+1/2,j-1/2} + (\pi\phi)_{i-1/2,j+1/2} - (\pi\phi)_{i-1/2,j-1/2}]$$

$$D_8(U) = \frac{1}{2\Delta x} [U_{i+1,j+1} - U_{i,j+1} + U_{i+1,j} - U_{i,j}]$$

$$D_9(V) = \frac{1}{2\Delta y} [V_{i+1,j+1} - V_{i+1,j} + V_{i,j+1} - V_{i,j}]$$

$$U = \bar{\pi}u$$

$$V = \bar{\pi}v$$

$$\lambda_{k+1/2} = \frac{1}{2}(\lambda_k + \lambda_{k+1})$$

$$\bar{\lambda}_{i+1/2,j+1/2} = \frac{1}{4}(\lambda_{i+1,j+1} + \lambda_{i+1,j} + \lambda_{i,j+1} + \lambda_{i,j})$$

$$C = \phi - RT^* \sigma \pi / P$$

$$w_{i+1/2,j+1/2,k} = \frac{1}{g} \left[ \left( \frac{\phi^n - \phi^{n-1}}{\Delta t} \right)_{i+1/2,j+1/2,k} \right. \\ + \frac{(\phi_{i+3/2,j+1/2} - \phi_{i-1/2,j+1/2})_k}{2\Delta x} \bar{u}_{i+1/2,j+1/2,k} \\ + \frac{(\phi_{i+1/2,j+3/2} - \phi_{i+1/2,j-1/2})_k}{2\Delta y} \bar{v}_{i+1/2,j+1/2,k} \\ \left. - \left( \frac{RT^* \pi \sigma'}{2P} \right)_k (\dot{v}_{k+1/2} + \dot{v}_{k-1/2})_{i+1/2,j+1/2} \right]$$